Characterization of innovative CFC/Cu joints by full-field measurements and finite elements

Roberto Fedele [a,*], Antonia Ciani [a], Luca Galantucci [a], Valentina Casalegno [b], Andrea Ventrella [b], Monica Ferraris [b]

[a] *Department of Civil and Environmental Engineering (DICA), Politecnico di Milano, Piazza Leonardo da Vinci 32, 20133 Milan, Italy*
[b] *Department of Applied Science and Technology (DISAT), Politecnico di Torino, Corso Duca degli Abruzzi 24, 10129 Turin, Italy*

1. Introduction

Among various refractory engineering materials, ceramic based materials are particularly attractive for many applications that require extreme damage tolerance and high temperature stability. Especially for space, terrestrial and energy applications, materials with the highest potential are fiber reinforced Ceramic–Matrix Composites (CMC), able to survive in extremely severe conditions, where not only temperature, but also wear, corrosion and variable and repeated mechanical loading represent the working conditions, see e.g. [1].

Particularly, CMC have been developed for fusion and advanced fission energy applications, due to their irradiation tolerance, and to safety features such as the inherent low activation/low decay heat properties and low tritium permeability. Among CMC, the Carbon Fiber reinforced, carbon matrix Composites (CFC) have been considered as possible plasma facing materials for the ITER Reactor [2]. In fact, CFCs were supposed to act as armor materials for the lower part of the vertical target of the divertor, expected to ensure structural functions while dissipating heat fluxes up to $20 \, \text{MW m}^{-2}$ under transient events.

To comply with the specific applications mentioned above, it is often mandatory to form bodies of complex shapes, but these cannot always be obtained by a direct sintering procedure. Thus, the particular characteristics of these ceramic materials can be fully exploited depending on the possibility to join the ceramic parts each other or to refractory alloys. In particular, one of the most critical points for the use of CMC is their joining to other ceramics or to metals.

In recent research works, some of the authors at Politecnico di Torino demonstrated the possibility of joining simultaneously CFC to Cu (or its alloys), by using one brazing alloy and heat treatment [3]. The proposed method is a simple and low-cost technique to join CFC composite to copper in both flat tile and monoblock geometries [4]. It does not require high pressure, and involves a lower temperature with respect to the joining process based on Cu casting. An excellent wettability of the brazing alloy on the CFC composite was obtained after modifying the composite surface by a high-temperature solid state reaction with chromium. A different procedure by the same authors allows one to perform direct casting of copper on the CFC surface previously modified by a chromium carbide layer [5,6].

An experimental campaign was performed on small samples joined by the one step-brazing process described above, subjected to several mechanical tests at room temperature such as torsion tests, single-lap and double-lap shear tests with and without offset, the standard test ASTM B898, see [3,6]. An unexpected scatter of data was found among these experiments, and further investigations by alternative approaches are therefore required.

* Corresponding author. Tel.: +39 022399 4275; fax: +39 022399 4220.
  E-mail addresses: fedele@stru.polimi.it, roberto.fedele@polimi.it (R. Fedele).

During the last decade no-contact, full-field 2D Digital Image Correlation (DIC) procedures are being widely applied to monitor experimental tests on a variety of heterogeneous samples at different observation scales both in laboratory and in situ, see [7–9]. As confirmed by several studies appeared in the literature (see e.g. [8,10]) high-accuracy, kinematic measurements acquired during mechanical tests significantly enrich the experimental information, allowing one to deeply investigate the conventional overall data and to monitor the "actual" boundary conditions prescribed to the sample. In particular, DIC approaches, which rest on a Galerkin finite element discretization of the displacement field, provide experimental information in a format fully consistent with the mechanical models in view of identification procedures, see e.g. [11].

The paper is organized as follows. Section 2 outlines the innovative joining technique and the laboratory production protocol for the joint prototypes. The experimental set-up for single-lap shear tests and the main features of the optical inverse analysis formulated as a 2D global Digital Image Correlation problem are described in Section 3. The heterogeneous finite element model developed in this study is described in Section 4, where the constitutive relationships for the adherents and for the finite thickness interface are detailed. The results of mechanical inverse analyses based on kinematic full field measurements and on a finite element model updating procedure are critically discussed in Section 5. Section 6 is devoted to closing remarks.

Notation. The objective function for the optical inverse problem and for the mechanical identification will be denoted by $\omega_f(\mathbf{u})$ and $\omega_u(\mathbf{X})$ (without square), respectively. Symbol G will denote a Hill parameter entering the plastic anisotropy matrix, not to be confused with the elastic shear modulus G. Acronyms DIC, ROI, FE will indicate the 2D global Digital Image Correlation procedure, the Region-Of-Interest, the Finite Element approach, respectively.

2. Innovative joining technique and sample preparation

The ceramic material considered in this work is a composite reinforced by a three dimensional carbon fiber texture (CFC), with commercial name SEP NB31. It was developed by the French company Snecma Propulsion Solide specifically for nuclear applications involving severe environments and high thermal conductivity requirements. The CFC SEP NB31 are produced starting from a NOVOLTEX® pre-form, with P55 ex-pitch fibers along the x direction and ex-Poly-Acrylo-Nitrile (PAN) fibers in the y direction; the perpendicular direction (z) is needling direction obtained with PAN fibers, as schematically shown in Fig. 1. NOVOLTEX® is the trade-name of SEP's three-dimensional carbon fabric. It is a 3D carbon non-woven preform construction made by an automatic technology.

The main problems in the development of the CFC/Cu joints are as follow: (i) the large thermal expansion mismatch, which is expected to generate high stresses along the joint during manufacturing and operation, being for the Cu alloy the thermal expansion linear coefficient α equal to 16×10^{-6} [K^{-1}], while that of CFC equals 2.5×10^{-6} [K^{-1}]; (ii) the fact that Cu does not wet carbon, which prevents direct casting. As for (ii), it is well known that the contact angle of molten copper on carbon substrate is about 140°. To tackle problem (i), a pure copper interlayer (OHFC, oxygen free high conductivity), 2 mm thick, is introduced before joining the mating surface of the CFC to copper. Such interlayer is expected to work as a soft pad allowing the above mentioned thermal expansion mismatches to relax.

As a preliminary treatment, the composites, cut into several pieces, were subjected to surface modification. Cr powders were deposited on CFC by the slurry technique, see [6,12], with the formation of a carbide layer ($Cr_{23}C_6$,Cr_7C_3) identified by X-ray diffraction. Cr-carbide-modified CFC appears to have obtained best results in terms of Cu wettability, if compared with Mo or W modified CFC. The thermal expansion coefficient of the Cr carbides lies between that of CFC and copper. Thereafter, for the CFC/Cu joint a commercial non-active brazing alloy was used (87.75 wt% Cu, 12 wt% Ge and 0.25 wt% Ni; Wesgo Metals). Further details on the brazing process can be found in [3,4]. In this study samples with the flat-tile geometry including the CFC/Cu joint were produced and characterized.

Fig. 2 shows the SEM image of a CFC/Cu joint obtained by the one-step brazing technique, in which the above mentioned intermediate Cr-carbide layer can be distinguished. The cracks and pores existing in the original composite substrate prior to joining are infiltrated by copper; no interfacial decohesion or cracking is noted in the joint microstructure. The Cr-carbide layer at the interface between CFC and Cu is about 20 μm thick and its thickness is almost constant along the joint line.

3. Experimental set-up and optical inverse problem

Significant difficulties were met for the mechanical assessment of the innovative joint due not only to the compact geometry and
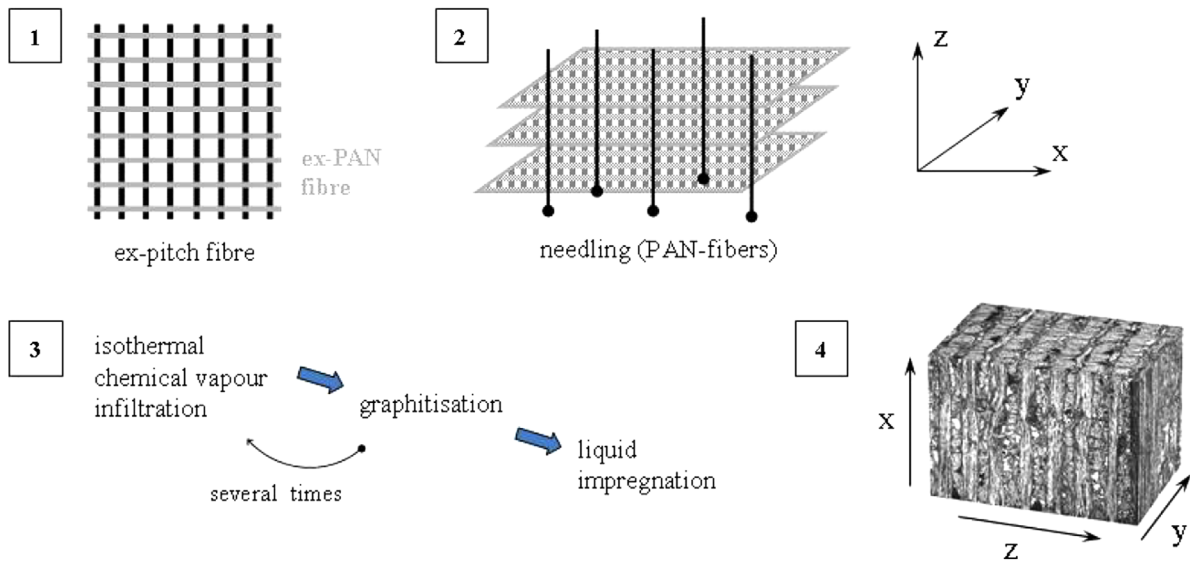

Fig. 1. Production stages of the composite material CFC SEP NB31, a carbon matrix ceramic reinforced by a three dimensional texture of carbon fibers.

reduced sizes of the prototypes, but mostly to the brittle response of the joint and to the properties of the CFC phase, which exhibits at the same time high strength and hardness and low fracture toughness. These conditions make prohibitive the recourse to both conventional screws and grips (with sharp edges) to fix the sample during the experiments.

In this study focus is posed on the single-lap shear test in compression, see Fig. 3. This configuration is a modified version of the ASTM standard [13], where the joint is included between two thin metal sheets loaded in tension. The single-lap shear test in compression requires a correct fixture-joining alignment to avoid bending stresses along the joint, see [14,15]. In comparison with other testing configurations, the single-lap shear test has provided less scattered results and does not requires notches.

The joined sample was glued to two loading fixtures by using an epoxy resin (Araldite®AV 119, Ciba-Geigy), whose polymerization was performed in air-oven at 130 °C for 1 h. For the experimental tests an electro-mechanical testing machine was used (Synthec D/10, MTS Corp. with 50 kN maximum capacity). The vertical displacement was applied to the sample with a crosshead speed of 8 μm/s, at a room temperature of 22–25 °C.

The post-mortem analyses of the fracture surface confirm the effectiveness of the adopted joining technique. In fact, crack mechanisms at the micro-scale involve (modified) composite material closely to the chromium carbide layer and/or the carbide layer itself, and not the carbide/braze interface or the braze itself (on the side of metal phase). Fig. 4 shows the typical fracture surfaces of a CFC/Cu joined sample subjected to a single-lap shear test: on both sides it is evident the presence of the composite (carbon fibers and matrix) that failed by interlaminar shear. Fig. 4(c) indicates that the fracture mechanism involves fiber pull-out, while in other regions of the fracture surface the presence of chromium carbide indicates that the cracks also propagated through the carbide layer.

Fig. 5 shows the reaction force recorded by the load cell as a function of the prescribed (machine) stroke displacement during the single-lap shear test. The apparent shear strength of the innovative joint is conventionally evaluated by assuming Mode II conditions throughout the experiment. At the peak the overall reaction force equals $F_{max} = 1419$ [N], and the average tangential stress at the interface can therefore be estimated as $\bar{p}_t = F_{max}/S \simeq 23.6$ [MPa], where $S = 60$ [mm^2] is the joined area. Especially in
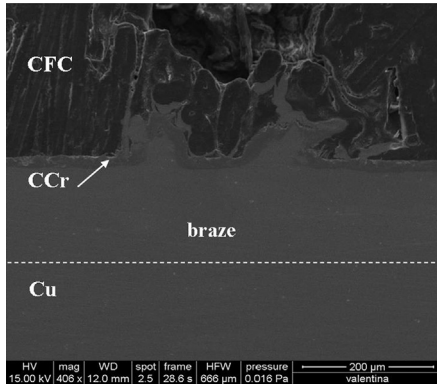

Fig. 2. SEM picture of a thin transversal section orthogonal to the joined surface. It is worth noting the formation of a chromium carbide (CCr) interphase which penetrates the highly porous microstructure of the composite CFC.
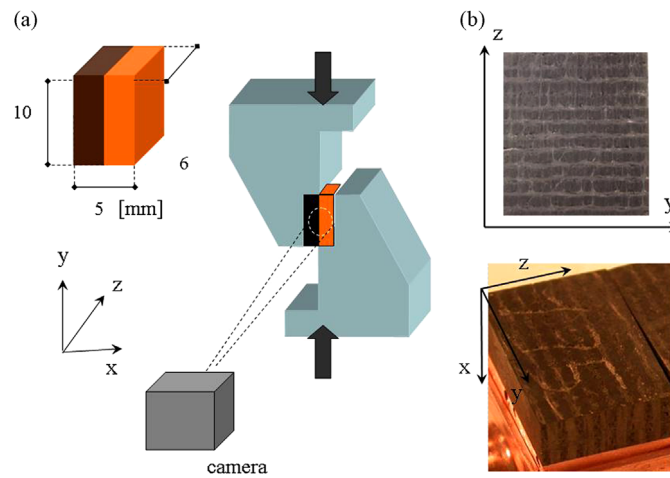

Fig. 3. (Color online) Adopted configuration for single-lap shear test in (a), and orientation of the monitored surface in (b), with respect to the anisotropy directions of the CFC phase within the joined sample. The CFC surface is brown colored with streaks, whilst Cu metal phase possesses a red-orange appearance.
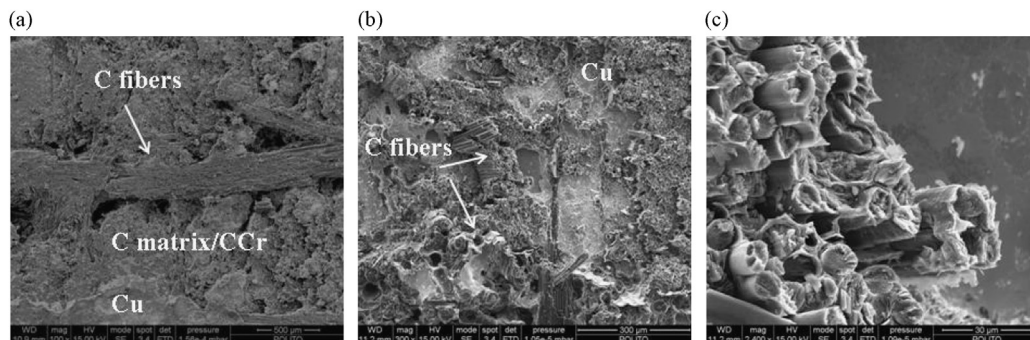

Fig. 4. Post-mortem analysis by SEM of the joint surface: in (a) and (b), pictures of the fracture surface on CFC and Cu side of the joint, respectively, in (c), detail of carbon fibers on Cu side of the crack surface.
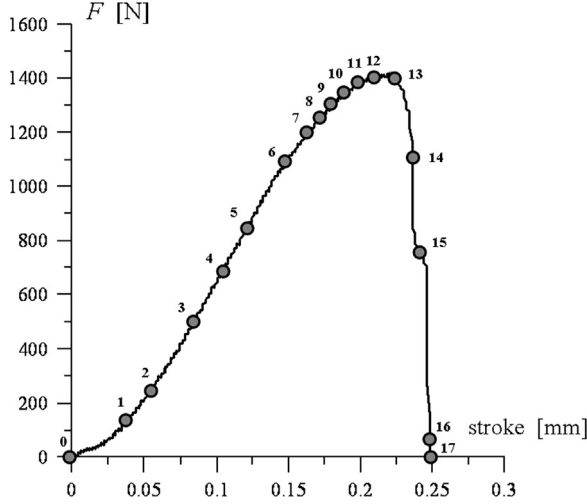
Fig. 5. Reaction force F as a function of the prescribed (machine) stroke during the single-lap shear test. Measurement instants at which digital images were selected for DIC analysis are marked by circles.

the presence of uncertain boundary conditions, no-contact, kinematic full field measurements are expected to provide useful information on displacement fields, on the basis of a sequence of 2D digital images acquired by a camera during the experiment.

A robust strategy for 2D global Digital Image Correlation (2D-DIC) is adopted herein, apt to provide accurate estimates of the in-plane displacement fields over the (flat) monitored surface of the joined sample during the shear tests. In what follows only a few hints are provided, whilst the interested reader is forwarded to [11,16,17] for further details on the present implementation.

For each gray-scale bidimensional image pair f_k and f_{k+1}, referred to in what follows as reference and deformed image, respectively, the in-plane displacement field $\hat{\mathbf{u}} = \{u_x, u_y\}^T$ is obtained as a solution of the following problem (nonlinear, nonconvex):

$$\hat{\mathbf{u}} = \arg\min_{\mathbf{u}} \left\{ \omega_f(\mathbf{u}) = \int_\Omega [f_k(\mathbf{x}) - f_{k+1}(\mathbf{x} + \mathbf{u})]^2 d\Omega \right\} \qquad (1)$$

in which the usual L^2-norm (squared) is used as error metric or similarity measure ω_f, which penalizes deviation from the brightness conservation (optical flux) assumption [8,9]. Domain $\Omega \subset R^2$ denotes herein the ROI, and spatial coordinates are gathered in vector $\mathbf{x} \equiv \{x, y\}^T \in \Omega$. The "optical" inverse problem in point turns out to be severely ill-posed, due to the nonlinear dependence of functional ω_f on the highly oscillating and noisy image texture and on spatially varying kinematic field $\mathbf{u}(\mathbf{x})$. By manipulations herein omitted for brevity (see e.g. [16]), the continuum problem in Eq. (1) can be posed in incremental form, and discretized by a Galerkin finite element approach, leading to a nodal vector of incremental displacements for the present image pair. Thereafter, at varying index k along a sequence of $n_t + 1$ digital images, a suitable updating scheme for the reference image and for the initial mesh can be applied, up to provide (consistently cumulated) nodal displacements at measurement instants $k = 1, \ldots, n_t$, referred to as $\mathbf{U}^{\exp k}$ in what follows.

The digital images were acquired by a conventional CCD camera (1.3 Mbyte, 1/3 inch sensor, 8 bit resolution depth) equipped with a Navitar© long distance objective. The estimated pixel size (footprint of the sensor pixel onto the object) amounts to 3.0 μm. From the acquired pictures a sequence of 17 images was selected (relevant measurement instants are marked by circles in Fig. 5) and processed by the 2D DIC code above described. The reference image with the finite element discretization adopted for DIC analyses are shown in Fig. 6(a), whilst Fig. 6(b) depicts the

final state of the monitored surface after collapse. Sample surface was not polished to avoid possible damage during sample preparation.

4. Heterogeneous model of the joined sample

To describe the multi-axial response of the metal phase (copper or its alloys) under the assumption of small strains and displacements, recourse is made to the closed-form, isotropic nonlinear model referred to as Ramberg–Osgood model [18,19]. Ceramic phase reinforced by carbon fibers (CFC) exhibits instead a marked anisotropy (both in the elastic and plastic regime), which is described by the anisotropic extension of the above model recently proposed in [20,21], where the interested reader is referred to for further details. The general anisotropic formulation is outlined in what follows, from which the isotropic response can be easily obtained as a particular case. The anisotropic Ramberg–Osgood model can be expressed through the following stress–strain relationship (derivable from a potential):

$$\boldsymbol{\varepsilon} = \boldsymbol{\varepsilon}_{el} + \boldsymbol{\varepsilon}_{pl} = \mathbf{C} : \boldsymbol{\sigma} + \frac{\alpha}{E_R}\left[\frac{\sigma_{eq}^{n-1}}{\sigma_0^{n-1}}\right]\mathbf{M} : \mathbf{s} \qquad (2)$$

where symbols $\boldsymbol{\sigma}, \mathbf{s} \equiv \boldsymbol{\sigma} - (tr\boldsymbol{\sigma}/3)\mathbf{1}, \boldsymbol{\varepsilon}$ denote the Cauchy stress, its deviatoric part, the linearized strain tensor (additively decomposed into an elastic and a plastic part, namely $\boldsymbol{\varepsilon}_{el}$ and $\boldsymbol{\varepsilon}_{pl}$), respectively, being $\mathbf{1}$ the second-order identity tensor, $\boldsymbol{\beta} : \boldsymbol{\gamma} \equiv \beta_{ij}\gamma_{ji}$ and $tr\,\boldsymbol{\beta} \equiv \beta_{ii} = \boldsymbol{\beta} : \mathbf{1}$; symbol $\mathbf{C}$ indicates the elastic compliance matrix. The generalized Mises equivalent stress is defined as $\sigma_{eq} \equiv (\mathbf{s} : \mathbf{M} : \mathbf{s})^{1/2}$, being $\mathbf{M}$ a fourth-order tensor governing the anisotropy of the yield surface and the direction of plastic flow, analogously to Hill criterion generalizing J_2-plasticity (see e.g. [18]). In the above Eq. (2), besides the anisotropic (elastic and plastic) matrices, four parameters σ_0 [MPa], E_R [MPa], α, n govern the smooth transition from the elastic behavior to the plastic response.

In Voigt engineering notation, the elastic compliance and the anisotropic plastic matrix (to be considered under plane stress conditions) are expressed as follows:

$$\mathbf{C} \equiv \begin{pmatrix} 1/E_x & -\nu_{yx}/E_y & -\nu_{zx}/E_z & 0 \\ -\nu_{xy}/E_x & 1/E_y & -\nu_{zy}/E_z & 0 \\ -\nu_{xz}/E_x & -\nu_{yz}/E_y & 1/E_z & 0 \\ 0 & 0 & 0 & 1/G_{xy} \end{pmatrix}$$

$$\mathbf{M} \equiv \begin{pmatrix} G+H & -H & -G & 0 \\ -H & H+F & -F & 0 \\ -G & -F & F+G & 0 \\ 0 & 0 & 0 & 2N \end{pmatrix} \qquad (3)$$

Fig. 3 shows the directions of anisotropy for the CFC phase, with reference to the adopted experimental set-up and the monitored sample surface (in the coordinate plane with axes x and y, as the FE model in Fig. 7), whilst z-axis turns out to be out-of-plane. For the fiber reinforced ceramic phase, parameters governing the elastic–plastic anisotropic response at low strains (see Table 1) are derived from the comprehensive handbook on ITER Materials [22] and adapted to the present formulation, when required integrated by literature data [23,24]. As well-known, the remaining ratios appearing in the compliance matrix Eq. (3) are easily specified by symmetry requirements, namely $\nu_{ij}/E_i = \nu_{ji}/E_j$ with $i, j = x, y, z$. For the Cu phase, the conventional isotropic response can be derived as a particular case from the above Eqs. (2) and (3) by assuming in the elastic compliance matrix $E_j = E$, $\nu_{ij} = \nu$, $G_{ij} = G \equiv E/[2(1+\nu)]$ for $i, j = x, y, z$, and, as for the Hill parameters, by setting $F = G = H = 1/2$ and $N = 3/2$. Table 2 shows the Cu mechanical parameters at low strains selected for the numerical simulations, on the basis of literature data (see [24–26]).
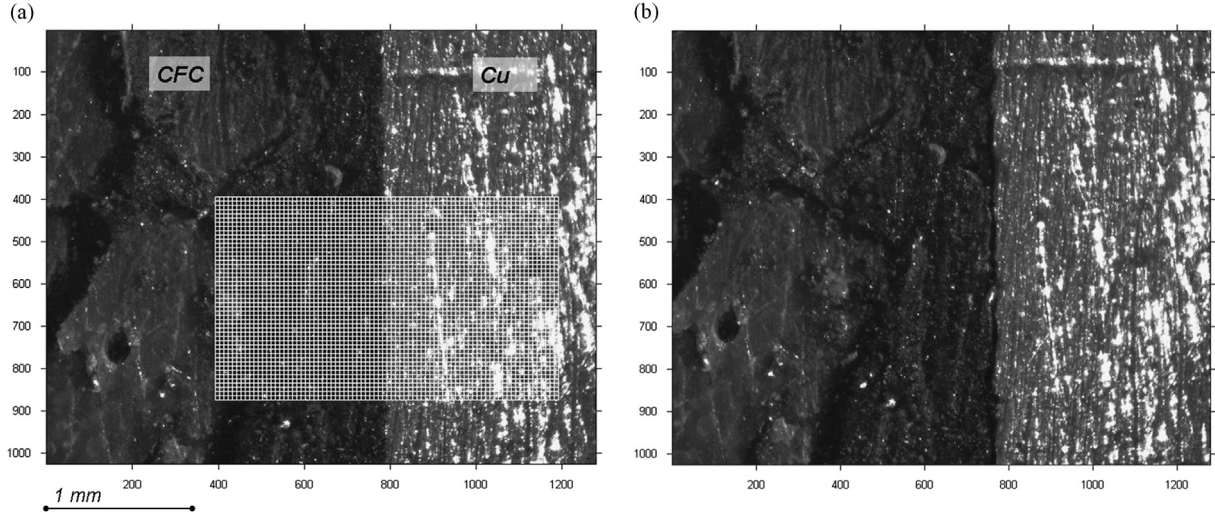
Fig. 6. Monitored surface of the joined sample subjected to single-lap shear test in the reference, undeformed state in (a), and at collapse with a complete joint failure in (b). Superimposed to the sample natural texture in (a), the finite element discretization for DIC is shown (with 10 pixel side elements).
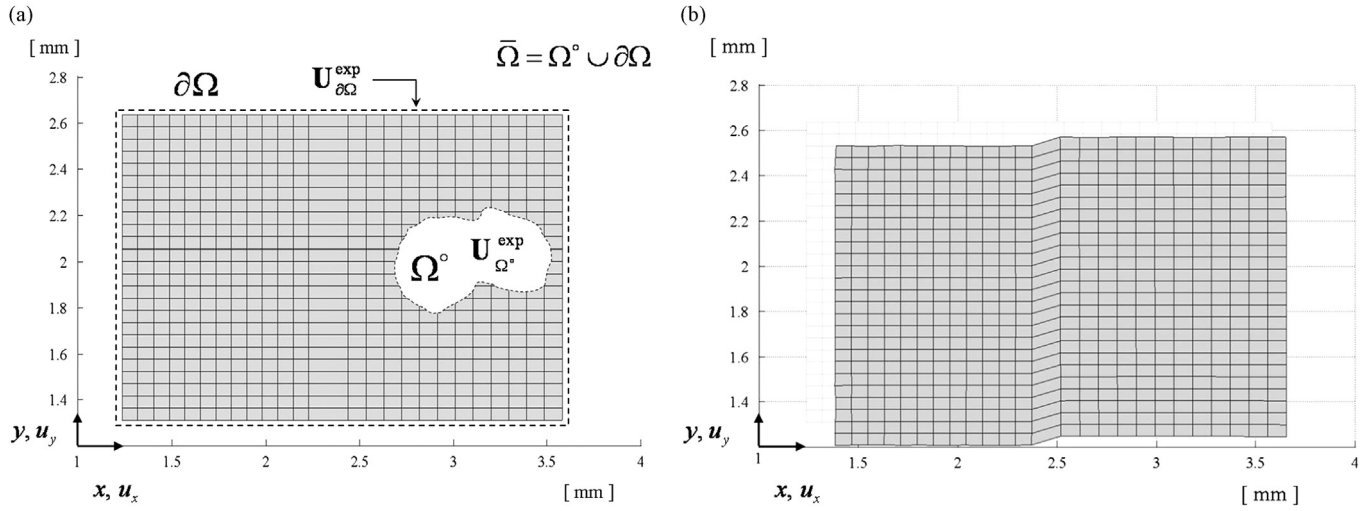

Fig. 7. Undeformed mesh adopted for the Region-Of-Interest Ω in (a) and, in (b), the deformed mesh at collapse (amplified ten times).

Table 1
Ceramic phase CFC SEP NB31: mechanical parameters at room temperature.

Elastic properties	Hill parameters for plastic anisotropy	Ramberg–Osgood parameters for the incompressible strains
$E_x = 107$ [GPa]; $E_y = 15$ [GPa]; $E_z = 12$ [GPa]; $\nu_{xy} = 0.10; \nu_{xz} = 0.20; \nu_{yz} = 0.20$; $G_{xy} = 10$ [GPa]	$F = 0.8; G = 0.5;$ $H = 0.5; N = 10$	$\sigma_0 = 100$ [MPa]; $E_R/\alpha = 2083$ [GPa]; $n = 7$

Table 2
Cu phase: mechanical parameters at room temperature.

Elastic properties	Ramberg–Osgood parameters
$E = 125$ [GPa]; $\nu = 0.34$;	$\sigma_0 = 300$ [MPa]; $\alpha = 0.06; n = 7$

The mixed-mode response of the innovative joint is described here by means of the interface model proposed in [27], to be regarded as a holonomic version of the Xu–Needleman exponential law. This law specifies a (coupled) relationship between normal and tangential tractions $\{p_n, p_t\}^T$ acting at the interface, and the dual (in the sense of work) kinematic quantities, namely the displacement discontinuities (or "jumps") $\{\Delta_n, \Delta_t\}^T$, see e.g. [28]. Interface

tractions possess the following closed-form expression:

$$
\begin{cases}
p_n = \dfrac{\phi_n}{\delta_n}\left(\dfrac{\Delta_n}{\delta_n}\right) \cdot \exp\left(-\dfrac{\Delta_n}{\delta_n}\right) \cdot \exp\left(-\dfrac{\Delta_t^2}{\delta_t^2}\right) \\[3mm]
p_t = \dfrac{2\phi_t}{\delta_t}\left(\dfrac{\Delta_t}{\delta_t}\right) \cdot \left(1 + \dfrac{\Delta_n}{\delta_n}\right) \cdot \exp\left(-\dfrac{\Delta_n}{\delta_n}\right) \cdot \exp\left(-\dfrac{\Delta_t^2}{\delta_t^2}\right)
\end{cases}
\tag{4}
$$

where ϕ_n and $\phi_t = r \cdot \phi_n$ denote the work-of-separation under peel (Mode I) and shear (Mode II) loading conditions; δ_n and δ_t denote critical opening displacements, at which normal and shear tractions under uniaxial (de-coupled) conditions achieve their peak values, respectively. The above cohesive relationship, which does not include a linear branch but is nonlinear starting from the origin, is governed by only three parameters, namely the peel work of

separation ϕ_n, the critical opening displacements δ_n and δ_t, being the (non-dimensional) ratio r assumed a priori (herein $r = 5$ is used). Unknown parameters governing the mechanical response of the joint are then gathered in vector $\mathbf{X} = \{\phi_n, \delta_n, \delta_t\}^T$. Due to the finite thickness of the joint, the compressive states with $\Delta_n < 0$ are described by a linear descending branch along the normal direction (with a continuous slope at the origin), decoupled from the tangential response (then assumed as if it were $\Delta_n = 0$, like in pure Mode II).

The heterogeneous model outlined above has been implemented in a Fortran 90 environment, coupled with Matlab® scripts for the identification procedure, see [10,28]. Exclusively a small rectangular subdomain approximately with 2.4×1.4 [mm] size, including the innovative joint and a part of the two adherents, was discretized by finite elements, see Fig. 7. Plane stress conditions were assumed, since the monitored surface of the sample turns out to be traction free. Conventional 4-node bilinear elements were used for the metal and ceramic adherents; at the micro-scale the joint was described by means of finite thickness interface elements equipped with the cohesive relationship in Eq. (4). An equivalent thickness of 200 μm was taken into account for the modeled joint due to the irregular profile of the physical interface (see Fig. 2), and to the presence, in a different percentage, of several compounds closely to it (chromium carbide, braze, and other) [3].

To assess the dependence of output quantities on parameter vector $\mathbf{X}$, recourse is made to sensitivity analyses. Fig. 8 shows the sensitivity with respect to the parameter vector $\mathbf{X}$ of the "constitutive" interface response in terms local tractions p_n and p_t, namely $\partial p_{n,t}/\partial \mathbf{X}^T$: in (a) and (b) under peel and shear (i.e. in pure Modes I and II, with $\Delta_t = 0$ and $\Delta_n = 0$), respectively, and under coupled conditions in (c), along radial paths at constant mixity ratio Δ_n/Δ_t. The code for forward FE analyses provides also the gradient of the displacement field with respect to the interface parameters, denoted by symbol $\partial \mathbf{U}^k/\partial \mathbf{X}^T$, easily computed by Direct Differentiation Method [10]. The "structural" sensitivity, concerning the vertical component of the displacement field computed by the FE model, is illustrated in Fig. 9 with reference to instant $k = 12$ during the test simulation. It is worth emphasizing that the measurable quantities with the highest informative content for identification purposes are located closely to the joint.

5. Mechanical inverse problem and discussion

To identify the mechanical parameters of the innovative joint, recourse is made to kinematic full-field measurements at the micro-scale, provided through a global DIC procedure as a solution of the optical inverse problem sketched in Section 3. As schematized in Fig. 7, displacements $\mathbf{U}_{\partial\Omega}^{\exp\ k}$, detected by DIC at each measurement instant k ($k = 1, \ldots, n_t$), were prescribed along the outer boundary $\partial\Omega$ of the discretized sub-domain to drive as Dirichlet conditions the FE simulations, see also [10]. Fig. 7 (b) shows the deformed finite element mesh at instant $k = 16$, with the initial configuration at the background. Displacements $\mathbf{U}_{\Omega^\circ}^{\exp\ k}$ concerning the interior part Ω° are instead used as comparison terms for identification purposes. The adherents, whose properties are assumed to be known a priori as outlined in Tables 1 and 2, play herein the role of a diffuse "load cell".

5.1. Deterministic approach

The optimal parameters governing the mixed mode mechanical response of the joint are obtained as a solution of the following nonlinear least square problem (see [30]):

$$\hat{\mathbf{X}} = \arg \min_{\mathbf{X}} \left\{ \omega_u(\mathbf{X}) = \sum_{k=1}^{n_t} \mathbf{R}_k^T \mathbf{R}_k \right\}$$
$$\mathbf{R}_k = \mathbf{W}_k^{-1/2} \cdot [\mathbf{U}_{\Omega^\circ}^{\exp\ k} - \mathbf{U}_{\Omega^\circ}^{\text{comp}\ k}(\mathbf{X})] \qquad (5)$$

The data included in the objective function are the kinematic residuals $\mathbf{R}_k$ at each measurement instant k, $k = 1, \ldots, n_t$, namely differences between the experimental displacements detected by DIC and their counterparts computed by the forward operator as a function of the parameter vector to identify $\mathbf{X}$. Weighting matrices $\mathbf{W}_k$ scale and make non-dimensional the kinematic residuals: their diagonal terms are set equal to the maximum experimental displacement in absolute value, separately for each component and time instant, to make comparable the different contributions. Herein $n_t = 16$ measurement instants have been selected, with $n_t + 1 = 17$ images (including the reference one), see Figs. 5 and 6.

The minimization process of the objective function $\omega_u(\mathbf{X})$ has been performed comparatively by the first-order Trust Region Method [29], using the sensitivity information, and by direct-search, zero-order Simplex method. The final parameter estimates $\hat{\mathbf{X}} = \{\phi_n, \delta_n, \delta_t\}^T$ are as follows: $\hat{\phi}_n = 0.106$ [GPa μm]; $\hat{\delta}_n = 0.665$ [μm]; $\hat{\delta}_t = 10.7$ [μm]. Under ideal Modes I and II (de-coupled) conditions, the maximum shear and normal traction predicted by the calibrated interface model amount to:

$$(p_n)_{max} = \frac{\phi_n}{e \cdot \delta_n} = 58.55 \text{ [MPa]}$$
$$(p_t)_{max} = \frac{r\phi_n}{\sqrt{e/2} \cdot \delta_t} = 42.61 \text{ [MPa]} \qquad (6)$$

Fig. 10 shows comparatively the experimental displacement U_y tangential to the joint, detected by DIC, and the relevant deformation scenario predicted by the calibrated FE model at different instants during the single-lap shear test ($k = 8, 12, 16$). At instants $k = 8$ and $k = 12$ the joint deformation turns out to be small, and rigid body motions can be noticed (with a few tenths of a degree rotation) endowed by noise fluctuations with maximum peaks of about 1.5 μm. It is worth noting that the experimental noise on boundary data (provided by DIC) determines oscillations of the displacement field computed by FE model, propagating from the outer frontier toward the inner discretized domain, worsened by the anisotropic nonlinear behavior of the CFC phase. In the deformation scenario at instant $k = 16$, see Fig. 10(c), the relative displacements between opposite sides of the joint become predominant, exceeding by far the magnitude of noise perturbations.

Fig. 11(a) shows the distribution of tangential traction p_t along the interface, computed by the FE model with the identified parameters $\hat{\mathbf{X}}$, and its evolution at different measurement instants during the test. The FE simulations reveal that in the same instants tensile tractions act normally to the joint, as shown in Fig. 11(b), and therefore more severe mixed mode loading conditions occur. At instant $k = 11$, before the peak of the overall reaction force (see Fig. 5), the calibrated model predicts a concave distribution of tangential stress along the joint, not exactly symmetric with a slight increase in the middle and the average value mean$\{p_t\} = 25.2$ [MPa]. In Fig. 11(b), the oscillations exhibited by the normal traction at instants $k = 8/11$ reflect the high stiffness of the joint along the normal direction, which significantly amplifies the effects of measurement noise on displacements. The x-axis also corresponds inside the CFC to P55 ex-pitch fibers with the higher stiffness. Moreover, at the same instants the left end of the joint turns out to be markedly compressed ($\Delta_n < 0$), with a sudden decrease of the normal traction.

At instants $k = 12$ and $k = 13$ (corresponding to the peak force along the overall plot), tangential stress reaches the values $p_t = 35.7$
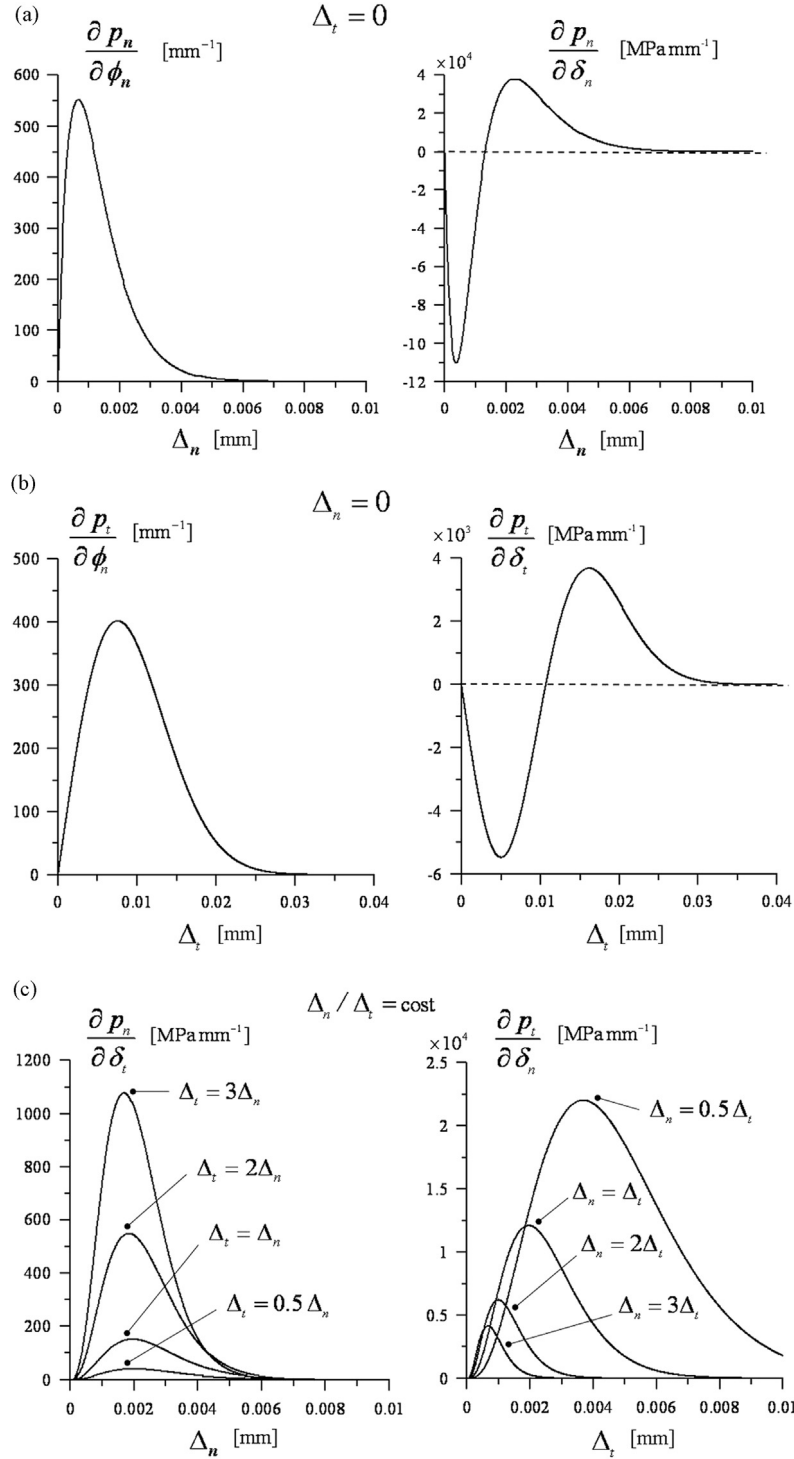
Fig. 8. Sensitivity with respect to parameter vector $\mathbf{X} = \{\phi_n, \delta_n, \delta_t\}^T$ of: (a) normal traction p_n, under Mode I loading conditions ($\Delta_t = 0$ and no dependence on δ_t); (b) tangential traction p_t, under pure Mode II ($\Delta_n = 0$ and no dependence on δ_n); (c) traction components under along radial paths at constant mixity ratio Δ_t/Δ_n.

[MPa] and $p_t = 40.2$ [MPa], respectively, closely to the left end of the modeled joint, whilst along the remaining part of the modeled interface it tends to progressively vanish. Measurement instants from $k = 14$ concern the post-peak branch of the overall plot: in Fig. 6(b) a macroscopic crack appears along the vertical joint, and FE simulation at instant $k = 16$ confirms that the joint turns out to be traction free. The normal traction p_n exhibits qualitatively similar profiles, with values slightly higher than the tangential component. In fact, at $k = 12$ and $k = 13$, normal stress reaches locally the values $p_n = 44$ [MPa] and $p_n = 41$ [MPa], respectively.

It is worth noting that, at instant $k = 11$ before the overall peak, the tangential traction predicted by the calibrated model is close to the maximum average stress $\overline{p}_t = F_{max}/S = 23.6$ [MPa]. At that instant, the maximum and the average values of tangential traction over the joint amount to max $\{p_t\} = 26.5$ and mean $\{p_t\} = 25.2$ [MPa], respectively. However, the agreement is merely numerical since tensile normal stresses act simultaneously along the joint and mixed mode conditions have to be properly considered. More closely to the overall peak, one instant later ($k = 12$, see Fig. 5), the calibrated FE model predicts a completely different distribution of shear
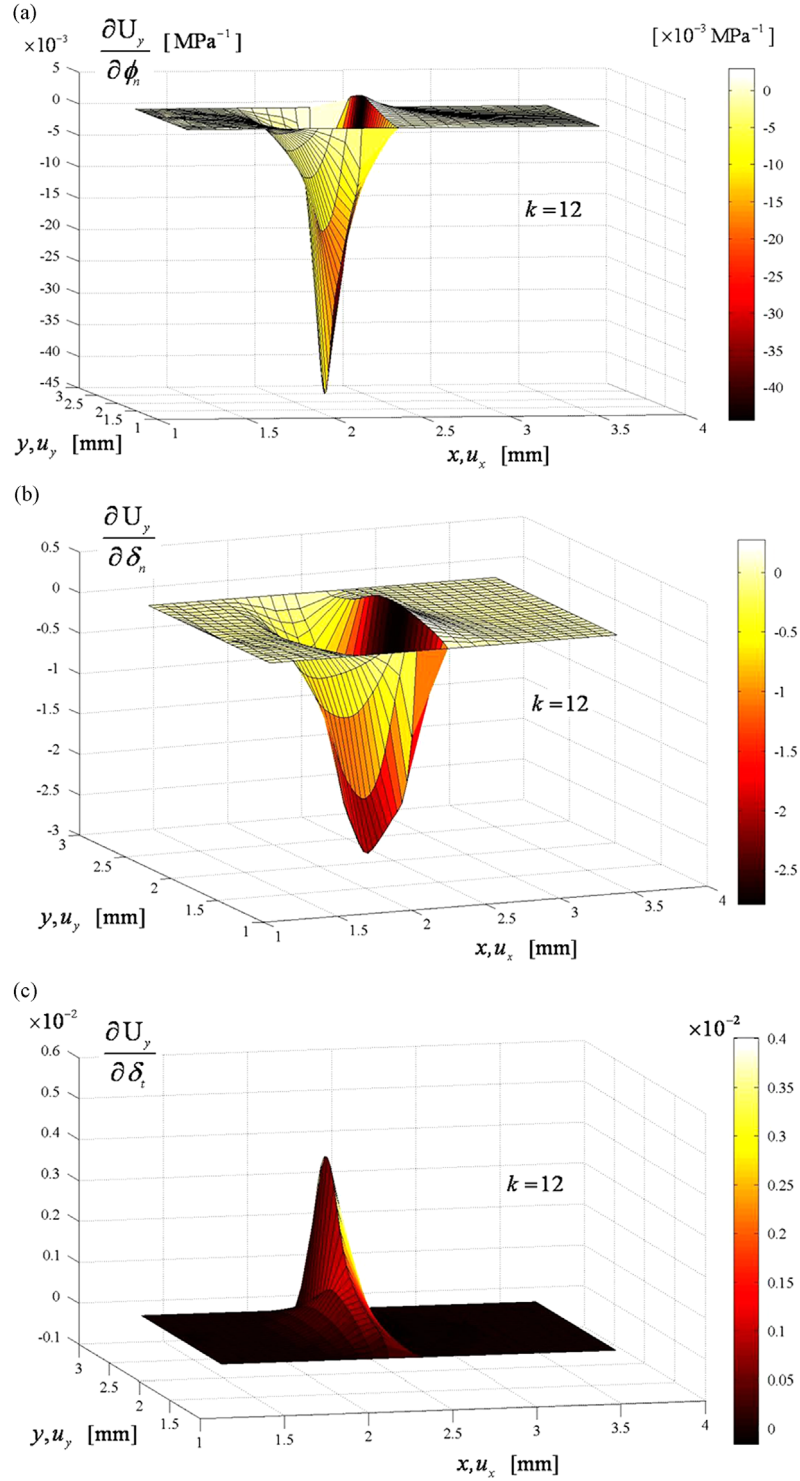
Fig. 9. Sensitivity of vertical displacement field U_y (parallel to the joint) at instant $k=12$ during the simulated experiment, with respect to parameters $\phi_n, \delta_n, \delta_t$ in (a), (b) and (c) respectively.

tractions: this circumstance indicates that a macroscopic crack was propagating in the meanwhile, leading to a sudden decrease of the joint binding capacity. Actually the uniform approximation of the tangential stress at the peak, referred as $\bar{p}_t$, relies upon a wrong assumption (as if a pure shear mechanism were activated) and even leads to grossly underestimate the joint shear strength predicted by the interface model under pure Mode II, reported in Eq. (6). Moreover, locally the maximum tangential stress $p_t = 40.2$ [MPa] is

achieved simultaneously with the overall peak, at instant $k=13$, but the relevant distribution along the joint is very irregular and far from the average prediction $\bar{p}_t = 23.6$ [MPa] mentioned above.

In the previous authors' works [3] the apparent shear strength of CFC/Cu samples was assessed on the basis of the overall reaction force comparatively by single-lap tests, with and without offset, and ASTM B898. A statistical analysis of the results therein provided led to an apparent shear strength (i.e. $\bar{p}_t = F_{max}/S$) of about 34 ± 4
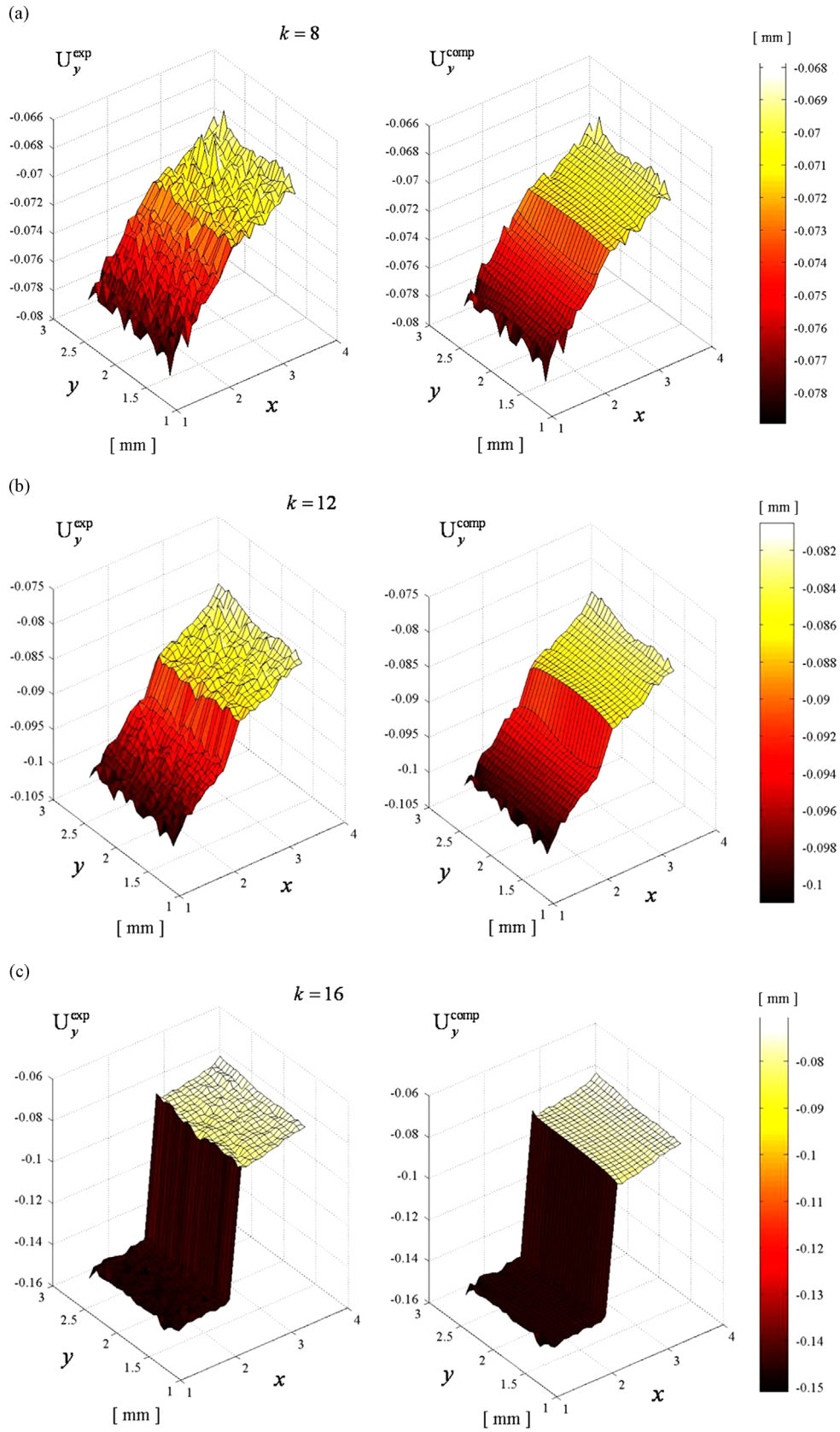
Fig. 10. Vertical displacement component U_y^{exp} (tangentially to the joint) estimated by DIC (on the left), and their counterparts U_y^{comp} (on the right) computed by the finite element model with calibrated mechanical parameters $\hat{\mathbf{X}}$, at instants $k=8$, 12, 16 in (a), (b), (c), respectively. For better visualization scales along z-axes at different instants are markedly different.
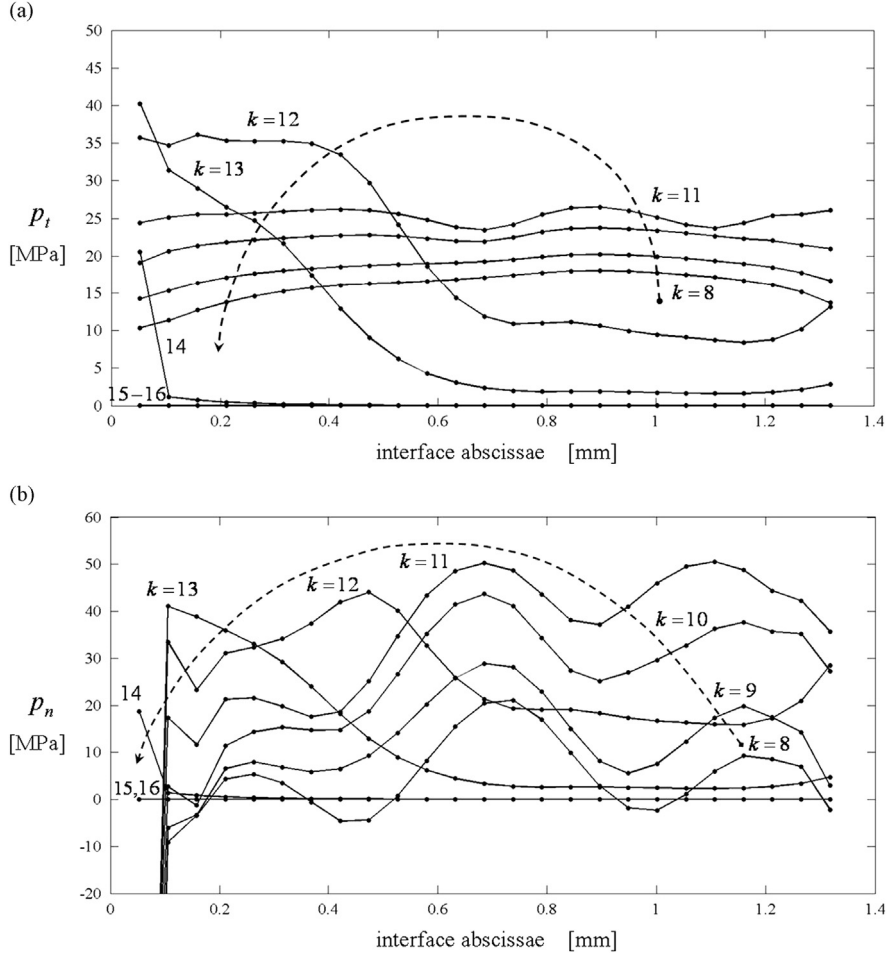
(a)

(b)

Fig. 11. Evolution of tangential and normal traction profiles along the joint in (a) and (b) respectively, computed by the FE model with calibrated interface parameters $\hat{\mathbf{X}}$, at different measurement instants k during the shear test simulation ($k = 1, ..., 16$).

[MPa]. It is worth noting that this value is comparable with the model prediction reported in Eq. (6) under ideal Mode II loading conditions, although it still underestimates it.

5.2. Perturbative analysis

The local methodology herein proposed rests on material properties for the adherents (Cu and CFC) assumed to be known a priori. Since the elastic–plastic response of the adherents is indeed uncertain, it is of interest to assess the dependence of final estimates on a perturbation of adherent properties, and to check the stability of the present inverse procedure quantifying the final uncertainty of joint parameters in vector $\hat{\mathbf{X}} = \{\phi_n, \delta_n, \delta_t\}^T$. To this purpose, recourse is made to the so-called σ-point strategy, already adopted in [30] to approximate the nonlinear transformation of a random vector. This strategy is constituted of the following operative steps: (i) each mechanical parameter governing the adherent behavior is given singularly a perturbation equal to $\mu_i \pm \sqrt{3} \cdot \sigma_i$, being μ_i its nominal (mean) value and σ_i the standard deviation, whilst the remaining properties, say $n_{adh} - 1$, are left equal to their nominal values; (ii) in this way, $2n_{adh}$ sets of perturbed properties for the adherent materials are generated; (iii) through the inverse analyses they are mapped into a cloud of image points $\hat{\mathbf{X}}_i$ in the parameter space $(\phi_n, \delta_n, \delta_t)$, each specifying a set of mechanical properties for the joint; (iv) on the basis of such discrete set of $2n_{adh}$ transformed points, the final mean value vector $\overline{\mathbf{X}}$ and the covariance matrix $\overline{\mathbf{C}}_X$ of interface mechanical parameters are computed by suitable sampling operators.

The σ-point procedure, resting on the nonlinear transformation of a discrete probability density distribution instead of a continuous one, can be proven to be accurate up to the fourth order, with a computational effort enormously lower than a Monte Carlo simulation, resulting prohibitive in high dimensions. Since properties of metals in general and in particular of pure copper (Cu) are known with accuracy, a standard deviation $\sigma_i = 1\%$ ($i = 1, ..., n_{adh}$) is considered, implying that 99% confidence interval for each property amounts to about $[\mu_i - 3\sigma_i, \mu_i + 3\sigma_i]$, i.e. $\pm 3\%$. The mechanical properties of the CFC are instead attributed a doubled standard deviation, i.e. $\sigma_i = 2\%$: consistently the 99% confidence amplitudes amount to $\pm 6\%$ around their nominal values. The histogram in Fig. 12 visualizes the percentage variation of the joint parameter estimate provided through inverse analysis when exclusively the i-th adherent property is perturbed, say $\hat{\mathbf{X}}_i$, with respect to the response $\hat{\mathbf{X}}$ achieved by the nominal value of adherent properties. The highest sensitivity of interface parameters can be observed with respect to the yield stress σ_0 of CFC and to its stiffness E_x along the direction orthogonal to the interface. However, under the present assumptions the maximum change in modulus for the parameter estimates does not exceed 2.5%, and therefore the inverse procedure turns out to be sufficiently robust and stable with respect to a priori information on adherent properties.

It is possible to visualize the uncertainty related to parameter estimates through confidence domains projected onto the coordinate planes, see Fig. 13. The $(1 - \alpha)$-confidence domain for a
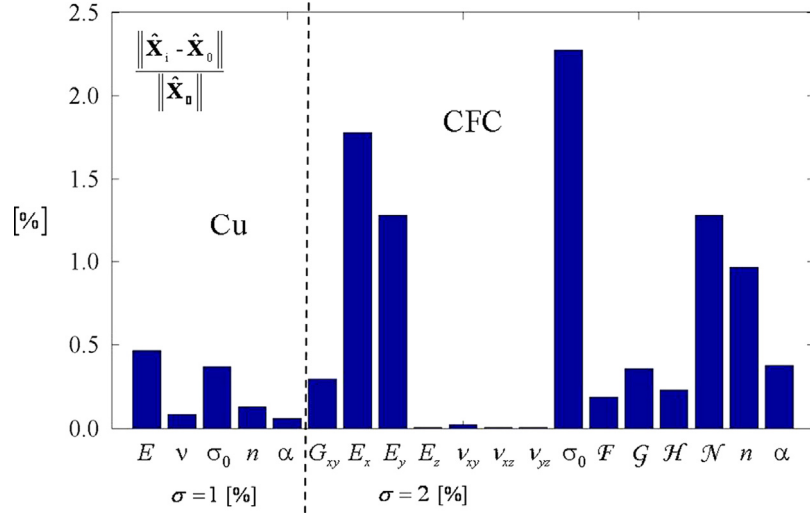
Fig. 12. Dependence in terms of percentage variation of estimated interface parameters $\hat{\mathbf{X}} = \{\hat{\phi}_n, \hat{\delta}_n, \hat{\delta}_t\}^T$ on adherent properties.
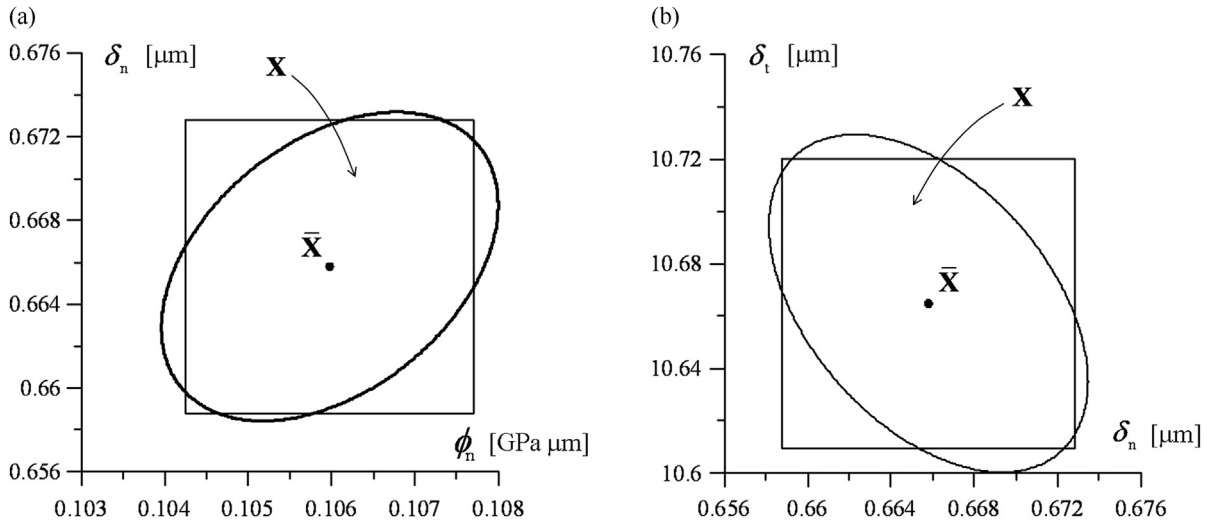

Fig. 13. 95% Confidence domains, as a consequence of uncertainty on adherent properties, for the estimated parameter vector $\overline{\mathbf{X}} = \{\overline{\phi}_n, \overline{\delta}_n, \overline{\delta}_t\}^T$, projected onto the coordinate planes (ϕ_n, δ_n) and (δ_n, δ_t) in (a) and (b) respectively: rigorous iso-density contours and equivalent Bonferroni's rectangles.

multivariate Gaussian variable is bounded by an ellipsoid, the center of which is located at the mean value vector $\overline{\mathbf{X}}$. These ellipsoids rigorously correspond to iso-density contours of the *a posteriori* probability density function (pdf), implicitly defined by the equation $(\mathbf{X} - \overline{\mathbf{X}})^T \mathbf{C}_X^{-1} (\mathbf{X} - \overline{\mathbf{X}}) = \chi^2_{n_X, 1-\alpha}$, being $\chi^2_{n_X, 1-\alpha}$ the $(1 - \alpha)$-quantile of the Chi-squared pdf with n_X degrees of freedom (herein $n_X = 3$), see also [31]. Moreover, parallelepidec domains in the sense of Bonferroni are derived herein, which are more practical for engineering purposes since they can be expressed as the Cartesian product of intervals along the coordinate axes (see [30]). In fact, the following bilateral inequality holds componentwise for the "actual" parameter vector, with a probability of at least $(1 - \alpha)$: $\overline{X}_i + z_{\alpha*} \cdot \sqrt{C_{X_{ii}}} \leq X_i \leq \overline{X}_i + z_{1 - \alpha*} \cdot \sqrt{C_{X_{ii}}}$ $(i = 1, 2, 3)$, being $z_{\alpha*}$ the normal distribution quantile with probability $\alpha* = \alpha/(2n_X)$. Indeed, for all the three mechanical parameters governing the mixed mode response of the joint, the uncertainty turns out to be rather low, with a coefficient of variation $\sqrt{C_{X_{ii}}}/\overline{X}_i$ of about 0.4%.

As a second stage, it is of interest to investigate how such uncertainty propagates from the joint parameter to output quantities

of nonlinear FE analyses (often referred to as "recalculated" data). To this purpose a 95% confidence envelope was built for both normal and tangential traction along the interface at test instant $k = 12$, see Fig. 14. Also in this case, the traction profiles exhibit a limited scatter, with an uncertainty width in average of about 2 MPa at each point of the joint. Therefore, we can consider the inverse procedure in point to be stable with respect to perturbations of adherent properties, and the parameter estimates thus achieved sufficiently robust.

6. Closing remarks

In this paper an improved 2D global Digital Image Correlation (DIC) code was synergistically combined with a finite element model updating procedure to assess the mechanical response of a joined sample subjected to single-lap shear test. The innovative joint was realized, according to a recently proposed technique, between the composite CFC SEP NB31, namely a carbon matrix ceramic reinforced by carbon fibers, and copper.

Peculiar difficulties were met for the mechanical assessment of the small joined prototypes, and recourse was made to an ad-hoc experimental set-up for single-lap shear test in compression. In
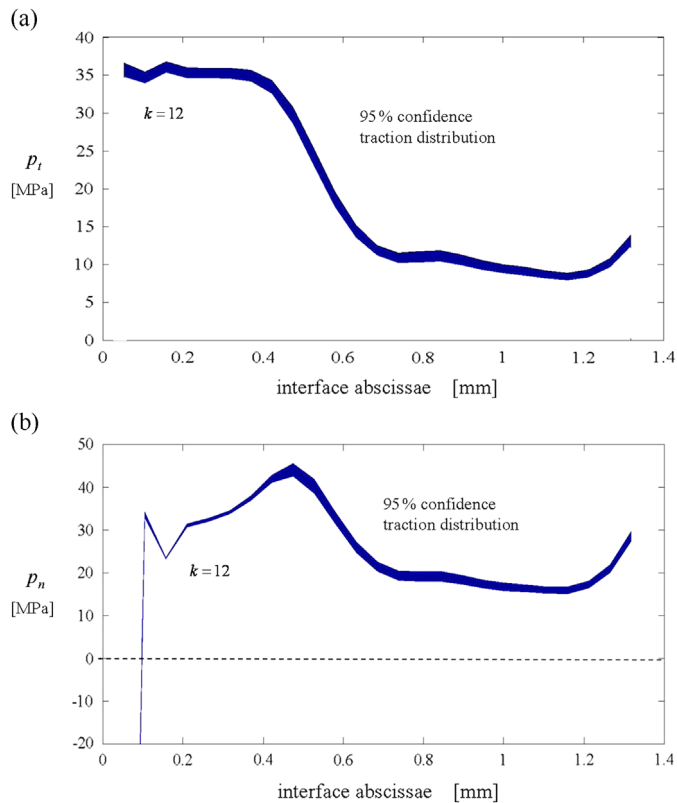
(a)

(b)

Fig. 14. 95% confidence intervals, as a consequence of uncertainty on adherent properties, for the estimated traction profiles along the joint, relevant to the tangential and normal traction in (a) and (b) respectively, at instant $k=12$ of the simulated test.

the presence of uncertain boundary conditions for the specimen, a local approach was considered, focusing on a small sub-domain optically monitored during the experiment. The simulations were driven by prescribed boundary conditions provided by DIC, whilst displacements in the interior domain were considered as reference quantities for identification. A perturbation study allowed to assess the stability of the overall procedure in the presence of uncertain adherent properties, assumed to be known a priori and playing the role of a diffuse "load cell".

Within industrial environments the average shear strength was so far considered the most meaningful parameter to assess the mechanical response of innovative joints. The strategy herein proposed allows one to reconstruct the traction profiles along the joint, to properly consider mode mixity generated by the adopted experimental set-up, and to estimate accurately the work-of-separation of the joint by exploiting images also along the post-peak branch of the experiment.

References

[1] D. Glass, in: Proceedings of XV AIAA Space Planes and Hypersonic Systems and Technologies Conference, 28/4–1/5 Dayton, vol. 2682, Ohio, USA, 2008, pp. 1–36.
[2] ITER Organization®, ⟨http://www.iter.org/⟩.
[3] M. Salvo, V. Casalegno, S. Rizzo, F. Smeacetto, M. Ferraris, M. Merola, J. Nucl. Mater. 374 (1–2) (2008) 69–74.
[4] V. Casalegno, M. Salvo, M. Murdaca, M. Ferraris, J. Nucl. Mater. 393 (2009) 300–305.
[5] P. Appendino, M. Ferraris, V. Casalegno, M. Salvo, M. Merola, M. Grattarola, J. Nucl. Mater. 222–329 (2004) 1563–1566.
[6] P. Appendino, M. Ferraris, V. Casalegno, M. Salvo, M. Merola, J. Nucl. Mater. 348 (2006) 102–107.
[7] R. Fedele, M. Scaioni, L. Barazzetti, G. Rosati, L. Biolzi, Cem. Concr. Compos. 45 (2014) 243–254.
[8] M. Grediac, F. Hild (Eds.), Full-Field Measurements and Identification in Solid Mechanics, 2013 (John Wiley and Sons, Hoboken, US; ISTE Ltd., London, UK).
[9] M.A. Sutton, J.J. Orteu, H. Schreier, Image Correlation for Shape, Motion and Deformation Measurements, Springer-Verlag, Heidelberg, 2009.
[10] R. Fedele, B. Raka, F. Hild, S. Roux, J. Mech. Phys. Solids 57 (7) (2009) 1003–1016.
[11] J. Réthoré, F. Hild, S. Roux, Comp. Meth. App. Mech. Eng. 196 (2007) 5016–5030.
[12] V. Casalegno, M. Salvo, M. Ferraris, Carbon 50 (2012) 2296–2306.
[13] ASTM D1002-05, Apparent Shear Strength of Single-lap-joint Adhesively Bonded Metal Specimens by Tension Loading [Metal-to-Metal], ASTM International, West Conshohocken, PA, USA, 2005.
[14] M. Ferraris, A. Ventrella, M. Salvo, M. Avalle, F. Pavia, E. Martin, Compos. B Eng. 41 (2010) 182–191.
[15] K. Schneider, B. Lauke, W. Beckert, Appl. Compos. Mater. 8 (2001) 43–62.
[16] R. Fedele, L. Galantucci, A. Ciani, Int. J. Num. Meth. Eng. 96 (12) (2013) 739–762.
[17] R. Fedele, A. Ciani, L. Galantucci, M. Bettuzzi, L. Andena, Fund. Inform. 125 (3–4) (2013) 361–376.
[18] J. Lemaitre, J.L. Chaboche, Mechanics of Solid Materials, Cambridge University Press, Cambridge, UK, 1994.
[19] W. Ramberg, W.R. Osgood, NACA Technical Note no. 902, 1943.
[20] Z.J. Moore, R.W. Neu, ASME J. Eng. Mater. Technol. 133 (3) (2011). (031001, 11 pp.).
[21] R. Mücke, O.E. Bernhardi, Comp. Meth. Appl. Mech. Eng. 192 (2003) 4237–4255.
[22] ITER Joint Central Team (JCT), Final Design Report ITER, Carbon Fibre Composites, Materials Assessment Report, ITER Engineering Design Activities Doc. Series, 2001.
[23] G. Pintsuka, J. Compan, T. Koppitz, J. Linke, A.T. Peacock, D. Pitzer, M. Rödig, S Wikman, Fusion Eng. Des. 84 (2009) 1525–1530.
[24] G. Bolzon, E.J. Chiarullo, V. Casalegno, M. Salvo, Strain 47 (2011) e474–e483.
[25] Y. Tamarin (Ed.), Atlas of Stress–Strain Curves, 2nd edition, ASM International, Ohio, US, 2002.
[26] A. Butts (Ed.), Copper. The Science and Technology of the Metal, its Alloys and Compounds, Reinhold Publishing Corp., New York, 1954. (American Chemical Society, Monograph Series. no. 122).
[27] M.J. Van den Bosch, P.J.G. Schreurs, M.G.D. Geers, Eng. Fract. Mech. 73 (2006) 1220–1234.
[28] N. Chandra, H. Li, C. Shet, H. Ghonem, Int. J. Solids Struct. 39 (2002) 2827–2855.
[29] The MathWorks Inc., Matlab 7.7 Optimization Toolbox, Prentice Hall, New York, 2008.
[30] R. Fedele, G. Maier, M. Whelan, Comp. Meth. Appl. Mech. Eng. 195 (2006) 4971–4990.
[31] R. Fedele, G. Maier, Meccanica 42 (2007) 287–402.